Role of initial precursors on the liquid-crystalline phase behavior of synthetic aluminogermanate imogolite nanotubes

Erwan Paineau, Stéphan Rouzière, Geoffrey Monet, Cristina Coelho Diogo, Isabelle Morfin, Pascale Launois

Graphical abstract:

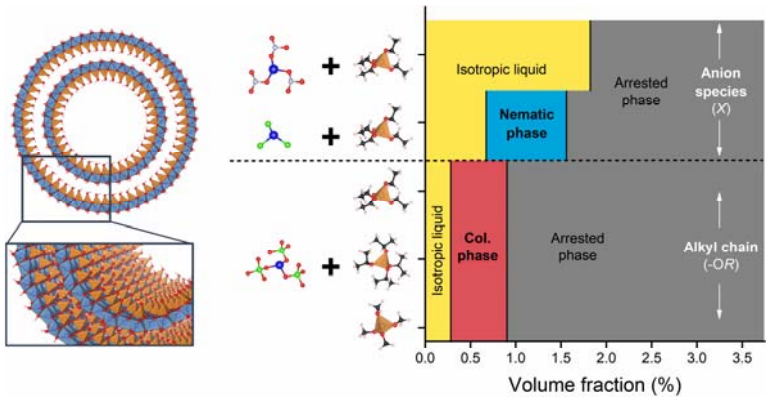

Highlights:

- Different double-walled aluminogermanate nanotubes (Ge-DWINTs) were synthesized.
- The nature of the aluminum salt alters the structural properties of Ge-DWINTs.
- Ge-DWINTs obtained from aluminum perchlorate precursor form a columnar phase.
- The use of chloride or nitrate salts induces only nematic or isotropic liquid.
- The different phase behaviors are due to structural defects in the nanotube walls.

Role of initial precursors on the liquid-crystalline phase behavior of synthetic aluminogermanate imogolite nanotubes

Erwan Paineau[1]*, Stéphan Rouzière[1], Geoffrey Monet[1], Cristina Coelho Diogo[2], Isabelle Morfin[3] and Pascale Launois[1]

[1] Laboratoire de Physique des Solides, CNRS, Université Paris-Saclay, F-91405 Orsay, France

[2] Institut des Matériaux de Paris Centre, CNRS, Sorbonne Université, 4 Place Jussieu, F-75005 Paris, France

[3] LIPhy, Univ. Grenoble Alpes, CNRS, F-38000 Grenoble, France

Corresponding author: erwan-nicolas.paineau@universite-paris-saclay.fr. Phone: +33 (0) 1 69 15 60 51

Abstract

Hypothesis: Synthetic imogolite nanotubes form stable colloidal dispersions that may also exhibit a rich liquid-crystalline phase behavior according to the nanotube length to diameter ratio. Anisometric double-walled aluminogermanate nanotubes are now readily available through hydrothermal treatment of germanium and aluminum precursors. This work aims to assess how the self-organization behavior of these nanotubes is influenced by the nature of the precursors.

Experiments: Five different samples were synthesized by changing the precursors involved in the formation of either inner or outer walls, then fully characterized. From series of aqueous dispersions prepared by osmotic stress, we evaluated the phase behavior by coupling polarized optical observations and small-angle X-ray scattering.

Findings: The formation of anisometric nanotubes is achieved whatever the initial conditions. Their structural properties are however affected by the nature of the aluminum salt. For nanotubes synthesized with aluminum perchlorate, the dispersions present an isotropic-to-columnar phase transition with a self-organization of the nanotubes over large distances. By contrast, nanotubes synthesized with chloride and nitrate salts form only nematic or isotropic liquids and tend to group together in bi-dimensional rafts. We suggest that the different phase behaviors are related at the first order to the presence of structural vacancies in the nanotube walls.

Keywords: Imogolite, nanotube, liquid-crystal, columnar phase, SAXS

1. Introduction

Liquid crystals (LC) form a wide class of materials that have found nowadays, numerous applications, from electro-optic devices to detergents or energy applications to name a few (Kato et al., 2018). They are also increasingly used in the "bottom-up" approach to nano-structuring. A liquid-crystalline phase is an intermediate state of condensed matter combining the fluidity of a liquid and the organization of its constituents as in a crystal (De Gennes and Prost, 1993). The so-called "lyotropic" liquid crystals occur when anisometric (i.e. rod-like or disk-like) objects are dispersed in a solvent. Therefore, the thermodynamic stability of lyotropic liquid-crystalline phases can be assessed from the range of their stability domain with the concentration of particles as a function of the salt concentration, pH or any other relevant physico-chemical parameter.

Colloidal dispersions of charged clay minerals exhibit various phase transitions, in particular the transition from a liquid state to an arrested phase (sol-gel transition) when the concentration of clay particles increases (Abend and Lagaly, 2000; Gabriel et al., 1996; Michot et al., 2004; Mourchid et al., 1995; Olphen, 1977; Ruzicka et al., 2011). Beyond this well-known phenomenon, the highly anisometric shape of clay nanoparticles makes them an ideal system for observing the spontaneous formation of LC phases, driven by excluded-volume interactions (Onsager, 1949). The formation of LC phases in dispersions of clay particles has attracted a considerable amount of attention in recent years (Miyamoto and Nakato, 2012; Paineau et al., 2013), probably because colloidal behavior of clay dispersions act as a key parameter for coating, thickening and thixotropic additives in industrial purposes (Carretero and Pozo, 2009; Harvey and Lagaly, 2013). LC phase transition has been observed not only in aqueous dispersions of exfoliated nontronite (Michot et al., 2006, 2008, 2013), beidellite (Paineau et al., 2009) or fluorohectorite (Hemmen et al., 2009; Miyamoto et al., 2010; Rosenfeldt et al., 2016) nanosheets but also in dispersions of clay nanorods or nanotubes, like sepiolite (Woolston

and van Duijneveldt, 2015; Zhang and van Duijneveldt, 2006), halloysite (Luo et al., 2013) and imogolite (Amara et al., 2013, p. 201; Kajiwara et al., 1986; Levitz et al., 2008).

Among all these systems, the case of imogolite clay nanotubes (INTs) is particularly interesting. Initially discovered in weathered volcanic soils (Yoshinaga and Aomine, 1962), research interest in these objects was greatly enhanced when they could be synthesized with high purity in laboratory conditions (Farmer et al., 1977; Poncelet, 2002). The structure consists of a curved dioctahedral $Al(OH)_3$ (gibbsite-like) sheet with isolated silicon tetrahedral sites connected to the octahedral vacancy by sharing basal oxygen atoms (Cradwick et al., 1972; Paineau and Launois, 2019). The protonation of internal silanol (≡Si-OH) but above all external aluminol groups (≡Al_2OH and ≡Al-OH) contribute to the specific surface charge of INTs with a positive outer wall and a negative inner cavity (Arancibia-Miranda et al., 2011; Gustafsson, 2001). Their unique porous structure with monodisperse diameter can be easily tuned according to the synthesis conditions (Amara et al., 2015; Picot et al., 2018). Many studies have focused on shaping novel synthetic imogolite-like nanotubes (Chemmi et al., 2015; Lee et al., 2014; Levard et al., 2011; Monet et al., 2018; Paineau, 2018; Yucelen et al., 2012b). Attempts to synthesize structural analogues of imogolite allowed to obtain INTs in large amounts when silicon is replaced by germanium precursors (Levard et al., 2008) while controlling their morphology as single (Ge-SWINTs) or double-walled nanotubes (Ge-DWINTs, see Fig. 1a) (Maillet et al., 2010; Thill et al., 2012).

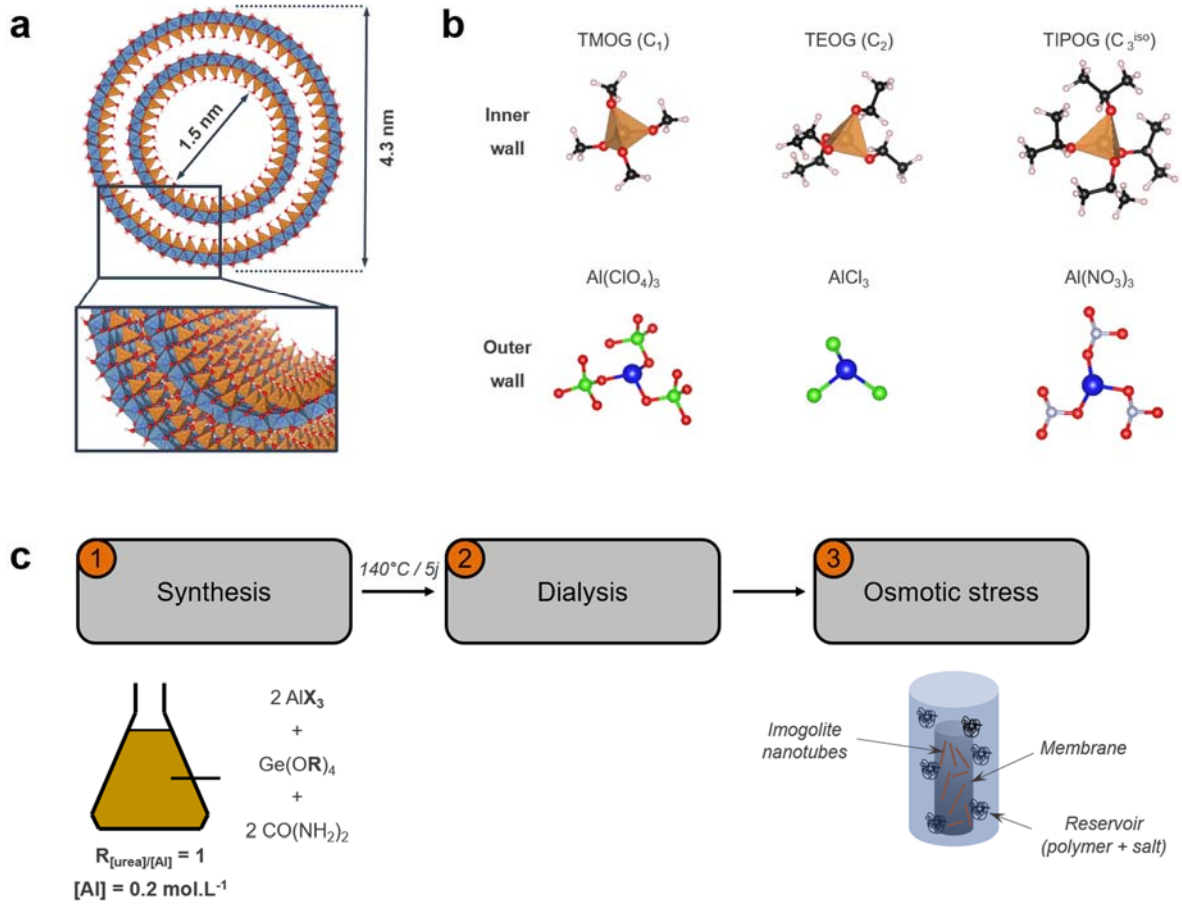

Fig. 1. (a) Structure and dimensions of a synthetic double-walled aluminogermanate imogolite nanotube (Ge-DWINT). (b) Initial precursors of the inner and outer walls: TMOG: tetramethoxygermane; TEOG: tetraethoxygermane; TIPOG: tetraisopropoxygermane. Color code: aluminum (blue); germanium (orange); oxygen (red); hydrogen (pink); chloride (green); nitrogen (grey). (c) Flowchart of the synthesis and sample preparation protocol. ***R*** corresponds to the alkyl chain of the alkoxide while ***X*** represents the anion of the aluminum salt.

Aluminogermanate nanotubes form stable colloidal dispersions through repulsive electrostatic interactions (Paineau et al., 2017, 2019) that may also display LC phases when the aspect ratio (nanotube length to diameter ratio) is large enough (Amara et al., 2013). Although aqueous dispersions of imogolite have been known to form a nematic phase for a long time (Kajiwara et al., 1986), recent studies have revealed the presence of an additional liquid-crystalline phase in dispersions of anisometric imogolite-like nanotubes (Paineau et al., 2016; Su et al., 2019). Small-angle X-ray scattering (SAXS) experiments demonstrated the hexagonal

columnar nature of this new phase that readily responds to high-frequency electric fields thanks to its very low concentration (~ 10 $g.L^{-1}$) (Paineau et al., 2016).

As shown previously (Amara et al., 2013; Paineau et al., 2016), Ge-DWINTs of 4.3 nm in diameter $\langle D \rangle$ and average length $\langle L \rangle$ higher than 100 nm can be synthesized using the homogeneous hydrolysis of precursors through thermal decomposition of urea $CO(NH_2)_2$, according to equation 1:

$$Ge(O\boldsymbol{R})_4 + 2Al\boldsymbol{X}_3 + 2CO(NH_2)_2 + 9H_2O \rightarrow (OH)_4Al_2O_3Ge + 4\,\boldsymbol{R}OH + 2CO_2 + 2H^+ + 4\,NH_4{}^+ + 6\boldsymbol{X}^- \quad (1)$$

Until now, only tetraethoxygermane (TEOG, R = C_2H_5) and aluminum perchlorate (X = ClO_4^-) have been employed to synthesize anisometric Ge-DWINTs according to equation 1. This single-step hydrothermal synthesis represents a straightforward approach for studying the role of initial precursors on the self-organization behavior of Ge-DWINTs. In this work, five different Ge-DWINT batches were synthesized following equation 1 to assess how the alkyl chain $\boldsymbol{R}$ or the anion species $\boldsymbol{X}$ of the aluminum salt (see Fig. 1b), preluding respectively to the formation of either inner or outer walls, may impact the LC phase behavior of anisometric Ge-DWINTs. The characterization of the different Ge-DWINTs were carried out by combining wide-angle X-ray scattering (WAXS), transmission electron microscopy (TEM), infrared (IR), electrophoretic mobility, nuclear magnetic resonance (NMR) and UV-vis spectroscopies, revealing that Ge-DWINTs are obtained whatever the synthesis conditions. Conversely, structural vacancies seem to occur depending on the nature of the anion. For each Ge-DWINTs batch, series of aqueous dispersions were prepared by osmotic stress at a fixed ionic strength to cover a wide range of concentration. Polarized optical observations and synchrotron-based SAXS experiments reveal that Ge-DWINTs synthesized from aluminum precursors other than perchlorate do not form the hexagonal columnar phase. Instead, samples synthesized from $AlCl_3$ display only a nematic phase, i.e. only a long-range orientational order of the nanotubes,

while Ge-DWINTs prepared from $Al(NO_3)_3$ do not form any LC phases. The impact of initial precursors is also reflected in the structural organization of Ge-DWINTs since the slope of the SAXS curves does not follow the same trends. Altogether, these results demonstrate that the initial anion species ***X*** is a preponderant parameter, which should be considered in all applications requiring the use of the colloidal properties of these peculiar nanotubes.

2. Materials and methods

2.1. Materials

Tetraethoxygermane (TEOG, ≥99.95%), tetraisopropoxygermane (TIPOG, >97%), aluminum nitrate nonahydrate ($Al(NO_3)_3.9H_2O$, >98%), aluminum chloride hexahydrate ($AlCl_3.6H_2O$, >99%), urea ($CO(NH_2)_2$, >99%), NaCl (≥ 99%), polyethylene glycol (M = 20000 $g.mol^{-1}$) and ethanol solution (96%) were purchased from Sigma Aldrich. Aluminum perchlorate nonahydrate ($Al(ClO_4)_3.9H_2O$, Reagent grade) was purchased from Alfa Aesar. Tetramethoxygermane (TMOG, ≥98%) was purchased from ABCR GmbH. All products were used as received.

2.2. Preparation of double-walled aluminogermanate Ge-DWINTs dispersions

All samples were prepared following the procedure described in Fig. 1c. First, Ge-DWINTs were synthesized using a simple one-pot method described earlier by Amara et al. (Amara et al., 2013). Germanium alkoxide was mixed at room temperature and under stirring with an aluminum salt solution (C_{Al} = 0.2 $mol.L^{-1}$) and a urea solution with a molar ratio [Ge]:[Al]:$[CO(NH_2)_2]$ = 1:2:2 (see equation 1). The choice of hydrated aluminum perchlorate instead of anhydrous salt has been made to minimize any risk of exothermic reactions when mixed with water. Hydrothermal treatment was then performed under autogenous pressure at 140°C for 5 days in a PFTE-lined acid digestion bomb (Zeoclave, Maximator, France). After cooling to room temperature, the resulting dispersions were dialyzed using semi-permeable membranes (Spectra/Por®, cut-off = 10 kDa) against ultrapure water (conductivity σ = 5.5 ×

10^{-3} mS.m^{-1}) until the conductivity of bath drops below 0.5 mS.m^{-1} (Paineau et al., 2013). As indicated above, Ge-DWINTs are usually obtained by using TEOG and aluminum perchlorate precursors. In this work, we followed two strategies (see Fig. 1b) either by using hydrated aluminium perchlorate precursors ($Al(ClO_4)_3.9H_2O$) and varying the length of the alkoxide chain (C_1, C_2 or C_3^{iso}), or by using TEOG and changing the anion species of the hydrated aluminum salt (ClO_4^-, Cl^-, NO_3^-). A total of five different Ge-DWINTs were synthesized and characterized (Table 1).

2.3. Characterization of Ge-DWINTs

Infrared (IR) spectroscopy was carried out in transmission mode using a Nicolet iS50 with a KBr beamsplitter and a DTGS/KBr detector. The samples were prepared in KBr pressed pellets (1 wt% of dry Ge-DWINTs powder). IR measurements with KBr pellet are preferred because they allow a better resolution on the structure of the nanotubes compared to the ATR mode (Liao et al., 2018). Spectra were acquired by averaging 64 scans at a resolution of 4 cm^{-1} in the mid-IR region (1300-400 cm^{-1}).

Wide-Angle X-ray scattering (WAXS) measurements on powder samples were performed on a rotating anode ($\lambda_{CuK\alpha}$ = 0.15418 nm) of the MORPHEUS platform of Laboratoire de Physique des Solides. Two-dimensional WAXS diagrams were collected on a MAR research X-ray-sensitive 345 mm plate detector with 150 µm pixel size, placed at a sample-to-detector distance of 250 mm. Powder samples were held in sealed 1 mm diameter borosilicate capillary tubes (WJMGlas/Müller GmbH, DE). Curves of scattered intensity I as a function of the scattering vector modulus Q ($Q = 4\pi/\lambda \sin(\theta)$ with 2θ the scattering angle) were obtained from the azimuthal angular integration of the scattering patterns using homemade software.

Transmission electron microscopy (TEM) observations were made on a JEOL 1400 microscope operating at 80 kV. Highly dilute dispersions of Ge-DWINTs were prepared at 1 mg.L^{-1} in ethanol and then a drop was laid on a carbon-coated copper grid. The length

distribution for each Ge-DWINTs batch was determined from the analysis of more than 300 nanotubes using Fiji software (Schindelin et al., 2012).

Solid-state ^{27}Al magic-angle spinning (MAS) NMR experiments were performed on a Bruker AVANCE III 700 spectrometer based on a 16.4T superconducting solenoid operating at ν_0 =182.47 MHz using commercial triple resonance Bruker MAS probe. Powder samples were transferred to ZrO_2 rotors with an outer diameter of 2.5 mm and spun at a MAS rate of 25 kHz. All ^{27}Al (spin I = 5/2) MAS NMR spectra were obtained by using short pulses (< π/8) for quantitative purposes. Nutation curves were first established by using a reference solution of 1M $Al(NO_3)_3$. All decomposition of spectra were performed using the DMfit software (Massiot et al., 2002).

Electrophoretic mobility was carried out on a Zetasizer Nano ZS (Malvern) operating at a fixed wavelength of 632 nm. Dilute aqueous dispersions of Ge-DWINTs (~ 2 $mg.L^{-1}$) flowed through a folded capillary polycarbonate cell. A potential of 150 V was applied between the gold electrodes of the cell. The electrophoretic mobility was determined as a function of pH by stepwise addition of a 0.1 $mol.L^{-1}$ NaOH solution (ΔpH ~ 0.5) under stirring.

UV-vis experiments were performed on a Cary 5000 spectrophotometer (Agilent) operating in dual beam mode and by using high precision quartz cell (Hellma, 10 mm light path).

2.4. Investigation of the phase diagram

For each synthesis, series of samples were prepared by osmotic stress (Fig. 1c) to obtain homogenous dispersions with varying concentration (Paineau et al., 2019). Dialysis membranes (Spectra/Por®, cut-off = 10 kDa) were filled with the initial stock dispersion of Ge-DWINTs and placed in 1L reservoirs. Simultaneously, the reservoirs were filled with solutions of different osmotic pressures prepared by dilution of PEG_{20000} in NaCl solution at fixed ionic strength ($IS_{[NaCl]}$ = 10^{-3} $mol.L^{-1}$) for all samples. After two weeks, the dispersions were recovered and their volume fractions ϕ were determined as $\phi = C/\rho_{INT}$, where C is the solid

concentration of Ge-DWINTs determined by weight loss upon drying and ρ_{INT} the density of a nanotube (~3.6 g.cm^{-3}) (Lee et al., 2020).

The birefringence of these samples was assessed first by naked-eye observations. For this purpose, the aqueous dispersions were transferred in 2 cm^3 glass vials (10 mm in diameter) and placed between crossed polarizers in a home-made setup. Macroscopic phases separations were observed using a Panasonic DMC-FZ18 camera. Optical textures were evidenced with a polarizing microscope (BX51-P, Olympus) equipped with a CCD camera. In this case, samples were introduced into flat optical glass capillaries (VitroCom, 0.2 x 2 mm), which were flame-sealed and stored vertically.

Small-Angle X-ray Scattering (SAXS) experiments on all series of samples have been realized on D2AM beamline at European Synchrotron Radiation Facility (Grenoble, France) at a fixed wavelength of 0.138 nm, using an ImXPAD (d5-S540) detector placed at a sample-to-detector distance of 2 m. The beamsize at the sample position was 200 µm². All dispersions were held in 1 mm diameter borosilicate capillary tubes (WJMGlas/Müller GmbH, DE) that were flame-sealed and stored vertically prior to experiments. As for WAXS experiments, angular integration of the scattering patterns giving the dependence of the scattered intensity versus *Q* was processed, using the PyFAI (Python Fast Azimuthal Integration) suite (Kieffer and Karkoulis, 2013).

3. Results and Discussion

3.1 Impact of the precursors on the structure of Ge-DWINTs

The synthesis of anisometric Ge-DWINTs by the urea method is a recent development (Amara et al., 2013), which has been achieved only in presence of TEOG and aluminum perchlorate precursors (sample 3). Using this sample as a reference, we tested the robustness of the chemical reaction depicted in equation 1 by changing either the alkyl chain of germanium alkoxide (samples 1-3) or the anion species of aluminum salt (samples 3-5) (Table 1).

Table 1. Structural characteristics of the different synthetic Ge-DWINTs.

Sample number	Ge precursor	Al precursor	Minimum length (nm)	Maximum length (nm)	Average length (nm)	PDI_L [a] (%)	Average diameter (nm)	PDI_D [a] (%)	Proportion of Al^{IV} (%)[b]
1	TMOG	$Al(ClO_4)_3$	16	590	99	80	4.41	11	0.2
2	TIPOG	$Al(ClO_4)_3$	15	1227	116	81	4.41	12	0.7
3	TEOG	$Al(ClO_4)_3$	14	870	88	85	4.38	11	0.6
4	TEOG	$AlCl_3$	10	578	100	81	4.35	11	0.7
5	TEOG	$Al(NO_3)_3$	12	363	66	62	4.44	13	0.3

[a] Polydispersity index PDI = $\sqrt{\langle X^2\rangle - \langle X\rangle^2}/\langle X\rangle$ with $\langle X\rangle$ being the average length L or diameter D of the nanotube. [b] Proportion of four-fold coordinated aluminum determined from the fit of NMR spectra at 70 ppm.

Fig. 2a presents IR measurements for the different samples. All samples display similar IR curves, whatever the synthesis conditions, with a peak at 915 cm^{-1} and a doublet at 830/805 cm^{-1} (Ge-O stretching modes) and several absorption bands at 690/555 cm^{-1} (Al-O stretching modes) and 468/420 cm^{-1} (O-Ge-O and O-Al-O bending modes), characteristics of the local structure in aluminogermanate imogolite nanotubes (Amara et al., 2013; Liao et al., 2019; Paineau et al., 2019; Thill et al., 2012; Wada and Wada, 1982). The peaks around 1100 cm^{-1} correspond to the presence of residual ClO_4^- ions, commonly observed for imogolite samples synthesized from aluminum perchlorate (Farmer et al., 1979; Paineau et al., 2017; Zanzottera et al., 2012).

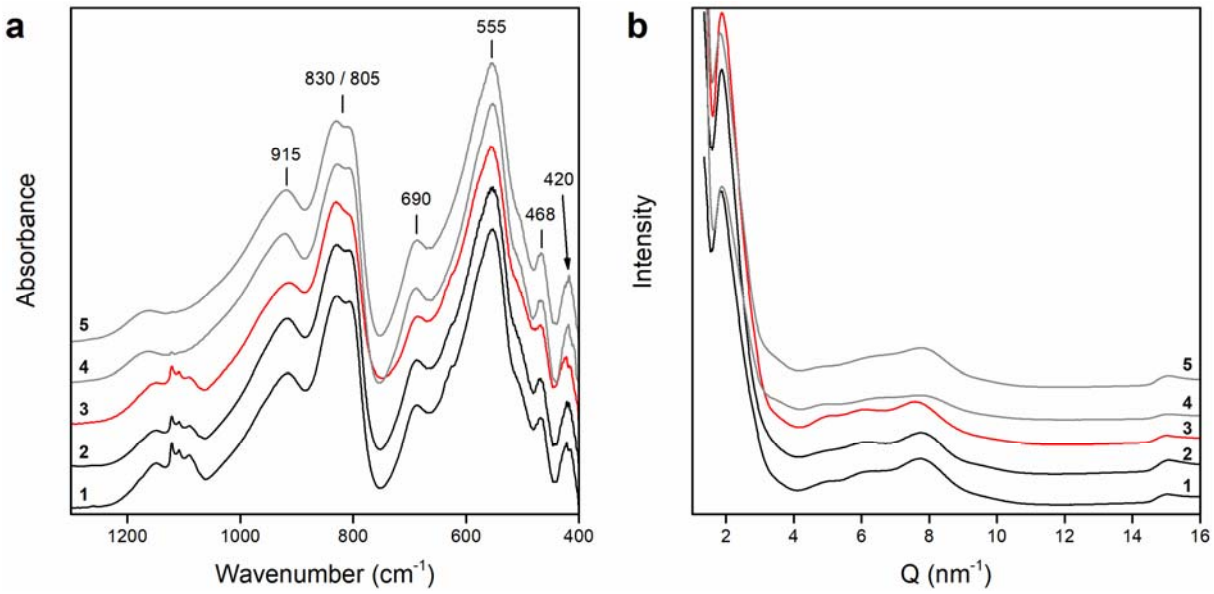

Fig. 2. (a) Infrared spectra and (b) WAXS diagrams for samples 1 to 5. The red curve corresponds to the reference Ge-DWINTs sample synthesized with TEOG and $Al(ClO_4)_3$. All curves have been translated for the sake of clarity.

WAXS diagrams of all samples are rather similar (Fig. 2b). The scattered intensity below 10 nm^{-1} consists of oscillations, whose intensity is enhanced above 5 nm^{-1}, in the *Q*-range characteristic of the mean inter-wall distance (Cambedouzou et al., 2009; Maillet et al., 2010). As with IR experiments, WAXS results show that the synthesis of Ge-DWINTs is successful either by changing the anion species, as also studied previously for synthetic Si-SWINT (Arancibia-Miranda et al., 2017; Bishop et al., 2013; Chemmi et al., 2015), or by using other Ge alkoxides (TMOG or TIPOG), which had never been attempted before. Furthermore, the presence of by-products such as boehmite AlO(OH) or gibbsite $Al(OH)_3$, commonly encountered in the synthesis of aluminosilicate imogolite nanotubes (Barrett et al., 1991; Chemmi et al., 2015; Picot et al., 2018; Tani et al., 2004; Thomas et al., 2012), are not detected. Interestingly, the positions of the minima below 10 nm^{-1} are not modified with respect to sample 3, indicating that the nanotubes walls have similar diameters and densities (Amara et al., 2013) regardless of the nature of the precursors (Fig. 1a,b). The sawtooth peak around 15 nm^{-1} is characteristic of the nanotube period (Monet et al., 2018), which is found to be equal to ~0.856

nm. Given the full width at half-maximum of the experimental resolution (FWHM ~ 0.13 nm^{-1}), X-ray scattering experiments can only be used to determine the nanotube length for tubes with length below 50 nm (Bousige et al., 2012). In the present case, sawtooth peaks are found to be similar in all samples, indicating average INT lengths larger than 50 nm.

Direct evaluation of the nanotubes length and diameter is achieved by using TEM observations. Fig. 3 and Fig. S1 (Supporting Information) display representative images for each Ge-DWINTs batch.

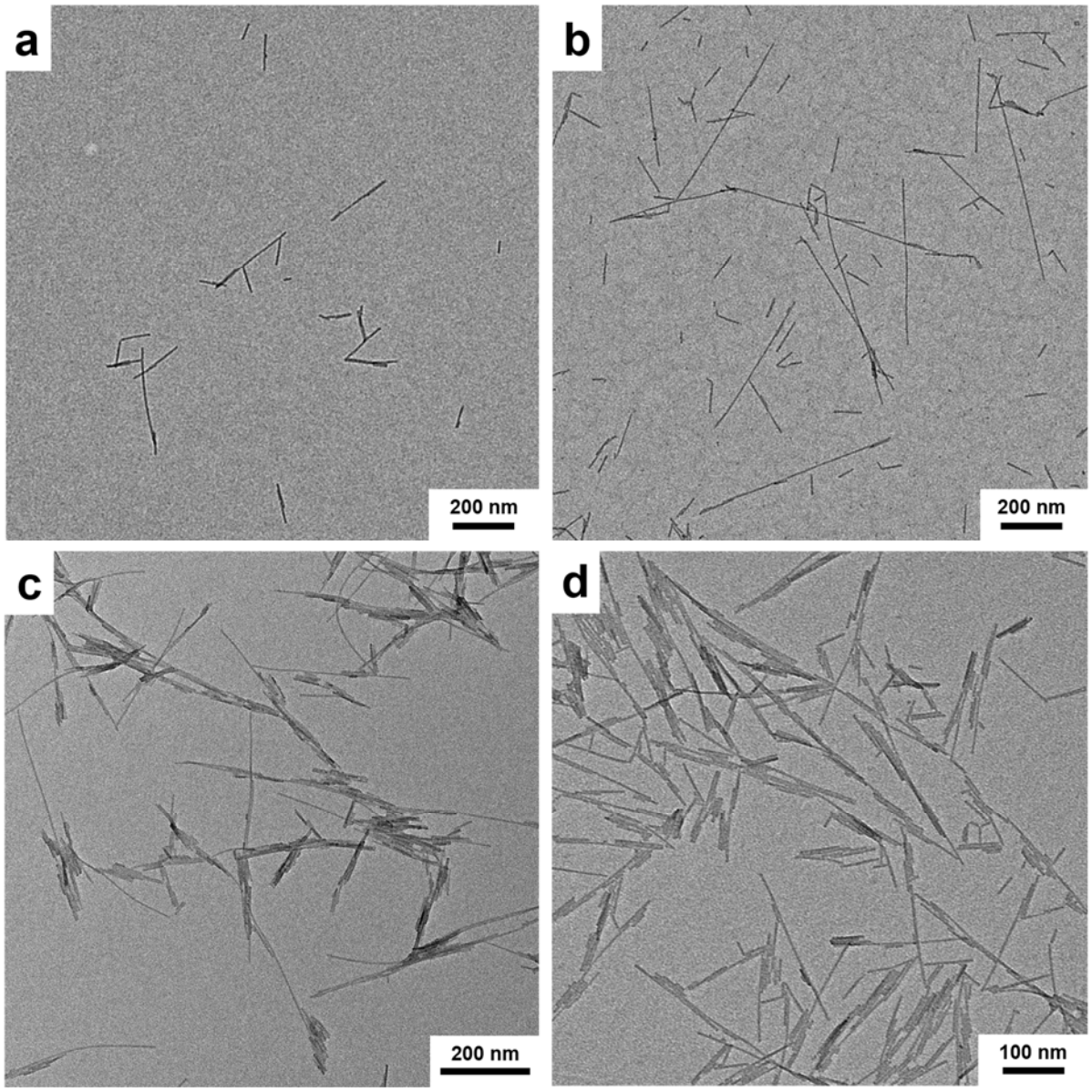

Fig. 3. Representative TEM images of Ge-DWINTs grids prepared from dilute dispersions in ethanol of as-synthesized batches. (a) Sample 1 (TMOG, $Al(ClO_4)_3$); (b) Sample 2 (TIPOG, $Al(ClO_4)_3$); (c) Sample 4 (TEOG, $AlCl_3$); (d) Sample 5 (TEOG, $Al(NO_3)_3$).

The associated length and diameter distribution histograms in Fig. S2 and S3 (Supporting Information) result from the analysis of at least 300 nanotubes per sample. Whatever the synthesis conditions, the length of Ge-DWINTs are extremely polydisperse, with polydispersity index (PDI) values of the same order as their average length (Table 1). Average lengths range from ~70 nm for sample 5 to ~120 nm for sample 2. Conversely, the average nanotube diameter remains mostly unchanged (~ 4.4 nm) and monodisperse (PDI ≤ 13%) regardless the samples (Table 1) in agreement with the WAXS results. It has been proposed that the presence of Cl^- and NO_3^- anions may inhibit the formation of silicon-based imogolite nanotubes (Farmer et al., 1983; Farmer and Fraser, 1979; Wilson et al., 2001). We show here that nanotube lengths are similar in all studied samples but well-dispersed individual nanotubes are observed only in TEM images from samples 1-3. For samples synthesized with Al sources other than perchlorate, Ge-DWINTs tend to bunch up in clusters of roughly parallel nanotubes (Fig. 3c,d). Such bunching may be induced by structural defects, which should modify electrostatic interactions (Teobaldi et al., 2009).

To test this hypothesis, we investigated the coordination environment of aluminum by ^{27}Al MAS NMR spectroscopy (Fig. 4a).

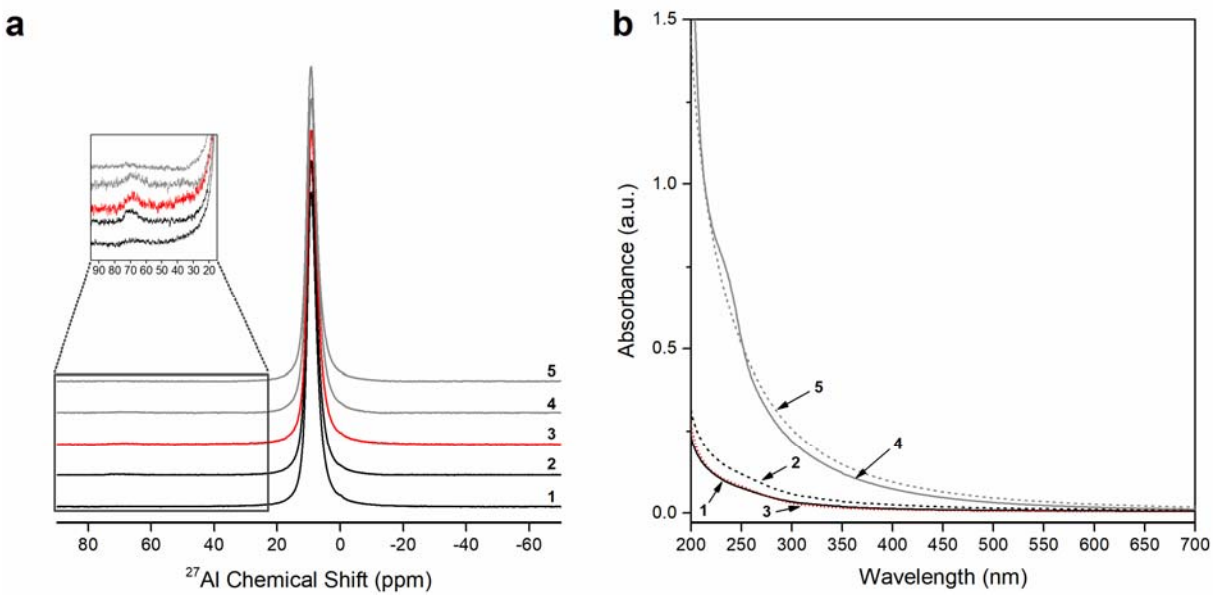

295

296 **Fig. 4.** (a) Solid-state ^{27}Al MAS NMR spectra of the different Ge-DWINT samples. The inset displays
297 a magnification highlighting the peak at 70 ppm related to tetrahedrally coordinated aluminum. All
298 curves have been translated for the sake of clarity. (b) UV-visible curves obtained on aqueous
299 dispersions of Ge-DWINTs (~10 $g.L^{-1}$). In both cases, the red curve corresponds to the reference Ge-
300 DWINTs synthesized with TEOG and $Al(ClO_4)_3$ (sample 3).

301 NMR spectra display a very sharp contribution located at 9.2 ± 0.1 ppm attributed to Al
302 atoms in octahedral coordination (Al^{VI}) as expected for the binding environment of Al in the
303 outer wall of imogolite nanotubes. This is consistent with previous studies on Si-SWINT
304 (Ildefonse et al., 1994; Yucelen et al., 2012b) and Ge-SWINT samples (Levard et al., 2010).
305 We could also detect an additional feature at ~70 ppm corresponding to tetrahedral aluminum
306 (Al^{IV}). This weak resonance feature may originate from a slightly disordered environment of
307 Al sites at the nanotube tip (Yucelen et al., 2012a). However, the tetrahedral Al defects
308 contribute here to less than 1% of the total signal and do not appear correlated with the nature
309 of the precursors (Table 1). In addition, structural defects arising from vacancies in the nanotube
310 walls can be present without drastically altering the peak related to Al^{VI} as shown for single-
311 walled imogolite nanotubes (Levard et al., 2010; Yucelen et al., 2012a). It is reasonable to
312 assume that such defect sites are formed during the synthesis of Ge-DWINTs.

Electrophoretic mobility of Ge-DWINTs samples synthesized with different aluminum salts was also investigated (Fig. S4, Supporting Information). All samples display a positive surface charge over a wide range of pH, a characteristic behavior of imogolite nanotubes (Gustafsson, 2001). The isoelectric point occurs at pH around 12, suggesting the nanotubes have only few external defects (Arancibia-Miranda et al., 2011). It is worth to note that the electrophoretic mobility measures the electric potential at the hydrodynamic slipping place and probes only the outer surface of the nanotubes (Bhattacharjee, 2016). We can thus conclude here that the structural defects do not imply modification of the outer surface properties with respect to electrophoresis. Finally, based on Levard et al. and Yucelen et al. publications (Levard et al., 2010; Yucelen et al., 2012a), the presence of defects on the internal part of the nanotubes walls, made of GeO4 tetrahedra, cannot be ruled out. On the grounds of the recent simulation investigations of Poli and co-workers (Poli et al., 2019), showing that structural vacancies in Si-SWINTs impact the low-energy tail in UV-vis spectra, we have thus measured the UV-vis spectra of all samples in liquid phase (Fig. 4b). We show in Fig. 4b that light absorbance is considerably increased, especially at low energy, by replacing perchlorate anions with chloride or nitrate anions, while the curves remain mainly unchanged when the length of the alkyl chain ***R*** is modified (samples 1-3). It can be inferred from the modifications of the spectra in the UV part that Ge-DWINTs present a larger amount of defects when synthesized from aluminum sources other than perchlorate. The resulting changes in the nanotubes electronic structure and in electrostatic interactions between nanotubes (Poli et al., 2019; Teobaldi et al., 2009) should lead to significant changes on the liquid-crystalline phase behavior expected for anisometric Ge-DWINTs.

3.2 Liquid-crystalline phase behavior

The different types of LC phases (nematic, lamellar, columnar or cubic) can be differentiated by combining polarized optical observations and SAXS experiments (Davidson

et al., 2018). Investigation of the phase behavior was conducted, for each Ge-DWINTs sample, on aqueous dispersions prepared by osmotic stress at a fixed ionic strength (IS = 10^{-3} mol.L^{-1}). This ionic strength allows for repulsive electrostatic interactions without aggregation phenomena between the nanotubes in dispersions (Paineau et al., 2017, 2019). Glass vials filled with Ge-DWINTs dispersions at different volume fractions were examined after one month, after which we no longer observed any evolution on the optical properties of the samples. Fig. 5 presents the birefringence of these samples assessed by naked-eye observations between crossed-polarizers.

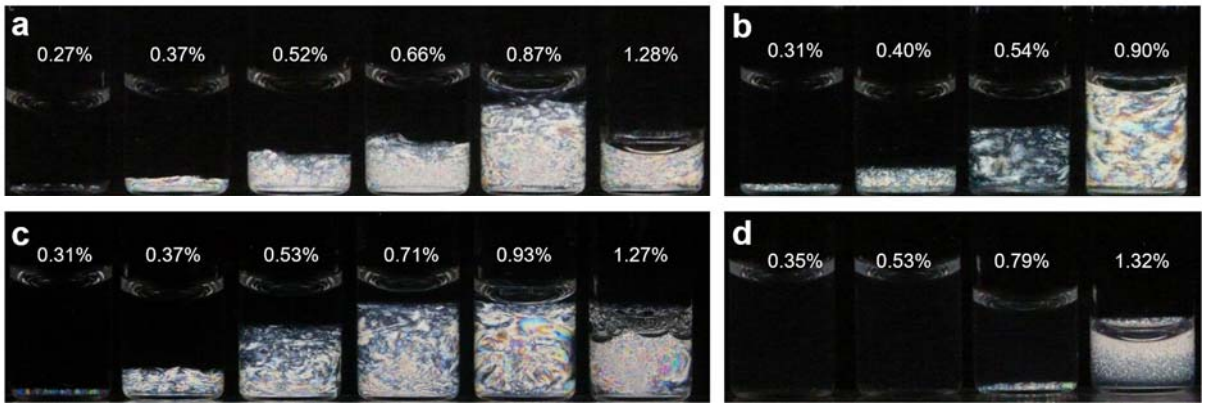

Fig. 5. Optical observations between crossed-polarizers of aqueous dispersions (IS = 10^{-3} mol.L^{-1}) of Ge-DWINTs as a function of the volume fraction ϕ (%). Syntheses using $Al(ClO_4)_3$ with (a) TMOG (sample 1), (b) TIPOG (sample 2), (c) TEOG (sample 3). (d) Synthesis using TEOG with $AlCl_3$ (sample 4).

Dispersions of Ge-DWINTs exhibit isotropic liquid phases at very low concentration ($\phi <$ 0.3%). Beyond a given volume fraction, we observe a spontaneous phase separation between a birefringent bottom phase and an isotropic (I) upper one delimited by a sharp interface. The isotropic phase exhibits flow birefringence when the vial is slightly shaken, indicating that nanotubes are not present exclusively in the birefringent bottom phase. The interface separating the two phases moves once the samples are tilted. This finding is a clear evidence that thermodynamic equilibrium is reached in the dispersions. As observed in other LC systems

(Kleshchanok et al., 2010; Woolston and van Duijneveldt, 2015), the amount of birefringent phase increases with the overall volume fraction, reflecting a first-order isotropic-to-liquid-crystalline phase transition. The visual phase observations also reveal that the range of the biphasic domain is not affected for Ge-DWINTs synthesized with different alkoxides (Fig. 5a-c), unlike when aluminum chloride or nitrate precursors were used. Indeed, the occurrence of a phase transition is shifted at higher volume fraction for sample 4 (Fig. 5d), while dispersions prepared from sample 5 remain isotropic over the entire concentration range studied.

To identify the nature of the birefringent phases, optical textures have been acquired by polarized optical microscopy (POM, Fig. 6 and Fig. S5 & S6, Supporting information). The insertion of a retardation filter allows identifying the preferred orientation of INT directors (nanotube axes) in the LC domains, ranging from parallel to perpendicular to the slow axis of the λ-plate with a change of the interference colors from blue to red, respectively.

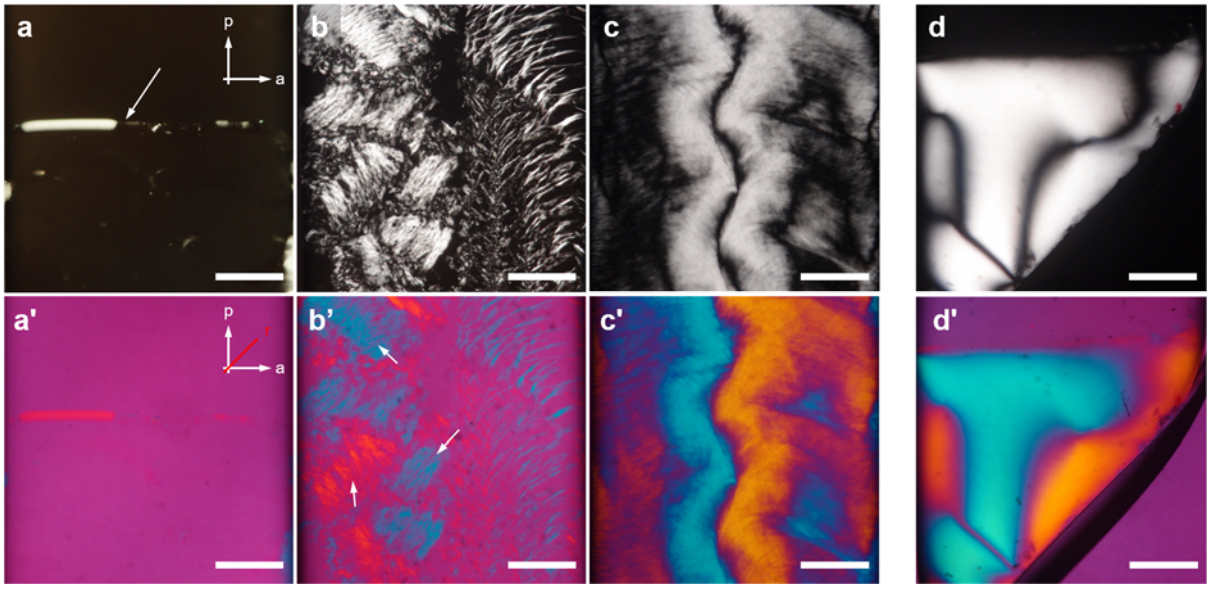

Fig. 6. Optical textures in polarized light microscopy of aqueous dispersions (IS = 10^{-3} mol.L^{-1}) of Ge-DWINTs without (top) and with (bottom) a retardation filter (λ-plate, 530 nm). The orientation of the polarizer and analyzer are indicated by labels *p* and *a*, respectively, while the red line represents the slow axis of the retardation filter *r*. (a-c) Case of sample 3 (TEOG, $Al(ClO_4)_3$) at different volume fractions: (a) ϕ = 0.37%, (b) ϕ = 0.53%, (c) ϕ = 1.27%. (d) Nematic Schlieren texture after phase

separation at the bottom of a flat capillary for sample 4 (TEOG, $AlCl_3$, ϕ = 0.79%). The scale bar represents 500 µm. The white arrow in (a) denotes the separation between the isotropic (top) and the liquid-crystal (bottom) phases.

POM images obtained for syntheses using $Al(ClO_4)_3$ precursors, i.e. samples 1-3, do not show the typical Schlieren texture related to the presence of topological defects in the nematic phase (N) like the one found for sample 4 in Fig. 6d-d'. Instead, pleated-ribbon-like domains are observed (Fig. 6b and Fig. S5 & S6) (Watanabe et al., 2001), in which the nanotubes are fully aligned as revealed by the modification of the optical path difference (white arrows in Fig. 6b'). This kind of texture suggests the presence of a columnar (Col) ordering as anticipated for dispersions of anisometric imogolite nanotubes at low volume fraction ($\phi < 1\%$) (Paineau et al., 2016; Su et al., 2019). At higher concentration, Ge-DWINTs dispersions form strong birefringent gels that display typical flow-alignment textures (Fig. 6c-c' and Fig. S5c-c'). The direct isotropic-to-columnar (I/Col) transition is somewhat puzzling. We assume this could be related to an intricate combination of polydispersity in length and effective electrostatic repulsions that can destabilize the nematic phase in favor of the columnar one (De Braaf et al., 2017; Hentschke and Herzfeld, 1991; Wensink, 2007). We also evidenced for biphasic samples close to the I/Col transition that spontaneous homeotropic alignment may occur in the columnar phase, i.e. the nanotubes are aligned with their long axis parallel to the optical axis of the microscope (Fig. 6a). As mentioned previously, the replacement of $Al(ClO_4)_3$ by $AlCl_3$ drastically affects the liquid-crystalline phase behavior by shifting the transition to higher volume fraction ($\phi \geq 0.79\%$, Fig. 5d). Moreover, the nature of the birefringent phase is also impaired since it is a nematic phase (Fig. 6d), i.e. exhibiting only a long-range orientational ordering of the nanotubes without positional ordering.

3.3 Self-organization of Ge-DWINTs

Small-angle X-ray scattering experiments were undertaken to assess in more details the structure of the different phases (Fig. 7a and Fig. S7 & S8 Supporting information). For samples 1-3, scattering intensity profiles in the isotropic phase show only broad modulations due to a short-range positional ordering of the nanotubes. By contrast, SAXS profiles in the birefringent phase display at least four sharp reflections, which shift to higher *Q*-values with increasing volume fractions as expected for a lyotropic LC (Fig. 7a and Fig. S7a,b). The relative *Q*-values of these peaks follow the ratio $1{:}\sqrt{3}{:}\sqrt{4}{:}\sqrt{7}$ that originates from the two-dimensional (2D) hexagonal reciprocal lattice peaks in the columnar phase (Camerel et al., 2002; Kleshchanok et al., 2012; Paineau et al., 2016).

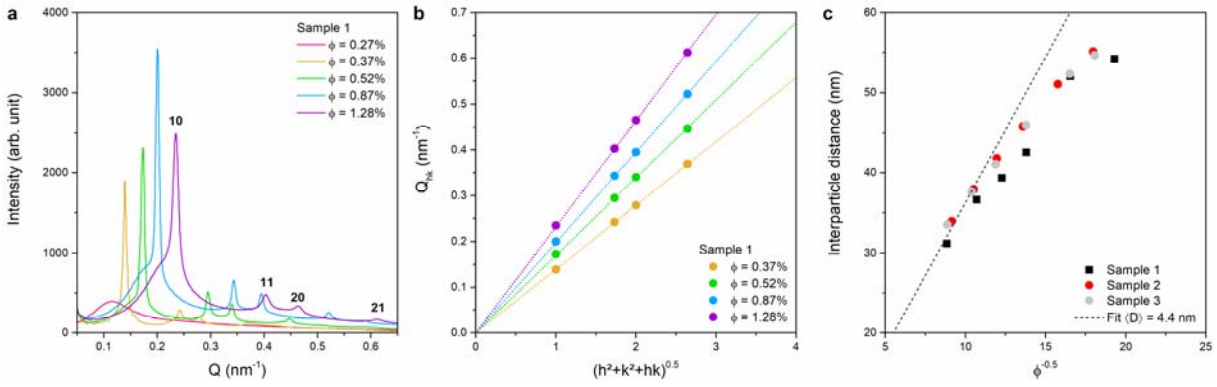

Fig. 7. (a) SAXS profiles of sample 1 (TMOG, $Al(ClO_4)_3$) at different volume fractions. The hk indices refer to the indexation of the Bragg reflections with a 2D hexagonal lattice of Ge-DWINTs in the columnar phase. (b) Corresponding plots of the *Q* vectors of the Bragg reflections vs. $(h^2+k^2+hk)^{0.5}$. (c) Evolution of the interparticle distance deduced from SAXS curves as a function of $\phi^{0.5}$. Dot curve corresponds to the model described in eq. 3 (see text for details).

Indexation of the SAXS reflections according to a hexagonal lattice was performed by plotting the *Q* vectors of the *hk* reflections at different volume fractions *vs.* $\sqrt{(h^2+k^2+hk)}$ (Fig. 7b) (Holmqvist et al., 1997). The straight lines illustrate the good agreement of the peak positions with the 2D hexagonal arrangement of the nanotubes. The hexagonal lattice parameter *a* is determined from the slope γ of these curves as:

$$a = \frac{4\pi}{\sqrt{3}\gamma} \quad (2)$$

The obtained values vary from 50 to 30 nm with increasing the volume fraction from 0.35 to 1.3 %, respectively, i.e. a minimum of 7 times the diameter of Ge-DWINTs. Such large center-to-center distances in the hexagonal columnar phase are not surprising for imogolite nanotubes. Even for an ionic strength of 10^{-3} mol.L^{-1}, the Debye screening length remains sufficient large (~ 10 nm) to prevent nanotubes aggregation (Paineau et al., 2016, 2019; Su et al., 2019). We also investigated whether the hexagonal columnar phase may undergo compression upon separation in the bottom of the capillaries. The hexagonal lattice parameter does not change regardless of the position of the X-ray beam in the sample (on nearly 30 mm), but we noticed that a broad modulation is always superimposed on the 10 peak of the hexagonal columnar phase and shift to higher Q-values with increasing ϕ. Fig. S7c (Supporting information) compares the SAXS profiles obtained in the two phases at coexistence for sample 1 at ϕ = 0.52%. The average inter-particle distance d, deduced from the position of the maximum of the modulation ($d = 2\pi/Q_{max}$), is 38 and 42 nm in the bottom and upper phases, respectively. We suggest that this peak is probably related to the contribution of nanotubes with short lengths (Paineau et al., 2019), whose aspect ratio is not large enough to form a liquid-crystal phase. Interestingly, for sufficiently high volume fractions (ϕ ~ 1%), aqueous dispersions are no longer liquid but form birefringent gels that retain the signature of the columnar phase (Fig. 6c). The persistence of the hexagonal columnar organization in an arrested phase is counterintuitive since we might have expected a decrease in nanotube ordering due to frustrated orientational and translational motion in such arrested phases. The comprehension of the underlying mechanisms is beyond the purpose of this article and will be the subject of further work. The evolution of the average interparticle distance exhibits a linear dependence with inverse square root of the volume fraction (Fig. 7c), typical of individual one-dimensional

objects (Belamie et al., 2004; Maier et al., 1992; Paineau et al., 2019). Such curve provides crucial information on the local structure of the dispersions. If we assume a 2D hexagonal configuration as the packing limit of the nanotubes, which seems reasonable for samples 1-3, the slope is directly related to the average diameter $\langle D \rangle$ of the nanotubes:

$$\text{Interparticle distance} = \left(\pi\sqrt{3}/8\right)^{1/2} \langle D \rangle \phi^{-0.5} \quad (3)$$

The experimental interparticle distances are well reproduced assuming an average outer diameter of ~4.4 nm for Ge-DWINTs as determined from TEM analysis (Table 1). The discrepancy with the model corresponds to the crossover toward a three-dimensional swelling of non-interacting nanotubes that should appear at low volume fraction (high $\phi^{-0.5}$ values).

Unlike samples 1-3, SAXS measurements performed on samples 4 and 5 do not show the Bragg peaks of the columnar phase but present several broad modulations related to a short-range positional ordering of the nanotubes (Fig. S8, Supporting information). In addition, the *Q*-dependence of the scattered intensity *I(Q)* for these samples is different from the first three samples (Fig. S7d, Supporting information). At sufficiently small wave-vectors, correlations between particles are negligible and the intensity is proportional to the form factor (Guinier regime) (Guinier et al., 1955). For samples 1-3, *I(Q)* is decreasing with a Q^{-1} dependence as expected for one-dimensional scattered objects while it follows a Q^{-2} slope for samples 4 and 5. The origin of this difference remains unclear but might be linked to the formation of bi-dimensional rafts of nanotubes as also indicated by TEM images.

Altogether, our results allow establishing a schematic phase diagram summarizing the role of initial precursors on the phase behavior of anisometric Ge-DWINTs as a function of the volume fraction (Fig 8).

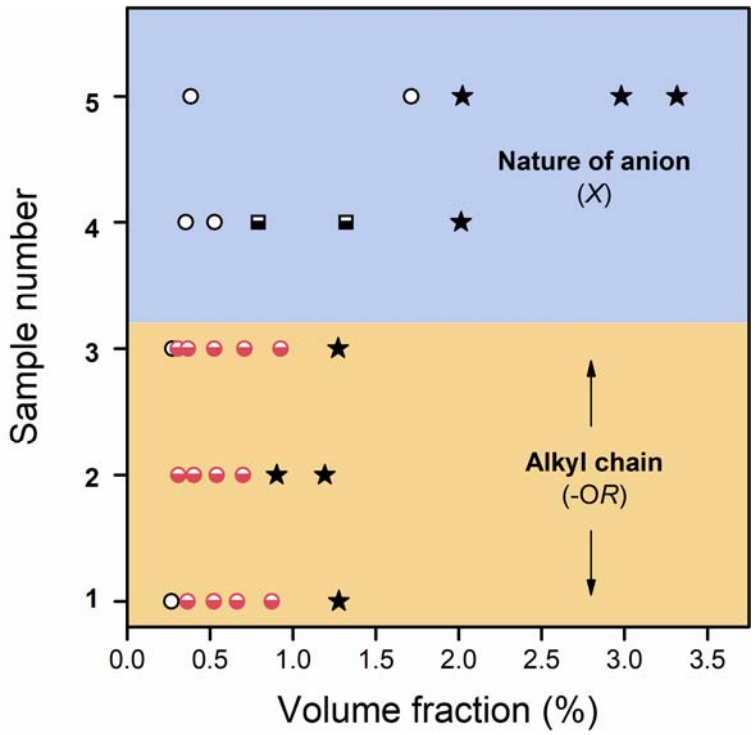

Fig. 8. Evolution of phase behavior as a function of volume fraction for the different Ge-DWINTs samples. Open circles: isotropic liquid; Half-filled red circles: isotropic-columnar coexistence; Half-filled rectangles: isotropic-nematic coexistence; Stars: arrested phase.

The occurrence of a hexagonal columnar phase and its extension remain unaffected regardless the alkoxide used. This is consistent with the results of the nanotube characterization, which are not significantly different between samples 1 to 3. It suggests that the length of the alkyl chain has a limited impact during the synthesis of these nanotubes. By contrast, we have demonstrated throughout this work that Ge-DWINTs synthesized from $AlCl_3$ or $Al(NO_3)_3$ solutions do not display the hexagonal columnar phase, but only nematic (sample 4) or isotropic (sample 5) liquids before the arrested phase. This decrease in structural organization goes beyond a modification of the aspect, these nanotubes still being anisometric. Furthermore, electrophoretic measurements suggest comparable charges of the outer surface of the nanotubes elaborated with different anion precursors (Fig. S4). We conclude that the nature of the anion leads to significant changes during the co-condensation of Ge and Al precursors by inducing structural defects occurring within the nanotube. We suggest that these defect-sites are certainly

at the origin of the formation of bi-dimensional rafts evidenced from TEM (Fig. 3c,d) and SAXS results (Fig. S7d). The presence of these bi-dimensional rafts hinders Ge-DWINTs to self-organize with long-range orientational and positional ordering as in the columnar phase.

4. Summary and conclusions

In summary, we demonstrated the reliability of producing anisometric Ge-DWINTs using a single-step hydrothermal synthesis described in eq. 1 by varying the initial precursors. We evidenced that the use of chloride or nitrate aluminum salts induces structural defects, most probably during the growth of double-walled aluminogermanate nanotubes. Optical observations and SAXS experiments confirm that Ge-DWINTs synthesized from aluminum perchlorate display the expected hexagonal columnar phase with a self-organization of the nanotubes over large distances. By contrast, nanotubes obtained with chloride and nitrate aluminum salts tend to group together in bi-dimensional rafts, which prevent them from forming highly ordered liquid-crystalline phases before the occurrence of the arrested phase. Our findings confirm that the nature of the initial anion ***X*** is a critical parameter, which apparently alters the structural properties of Ge-DWINTs whereas the length of alkoxy group (C_1, C_2 or C_3^{iso}) of Ge precursors does not. This is probably related to the lower complexing ability of perchlorate anions compared to chloride or nitrate (Chemmi et al., 2015; Farmer and Fraser, 1979). Consequently, the liquid-crystalline properties of anisometric Ge-DWINTs can be adjusted by changing the initial conditions of the syntheses. Experimental quantification of structural defects in these complex nanostructures is an issue that needs to be addressed if we want to better understand and therefore predict the electrostatic interactions between these nanotubes. Furthermore, these experiments also evidence an intriguing direct I/Col phase transition, which may open new research directions from a fundamental point of view. In addition, the large extension of the hexagonal columnar phase domain may provide higher flexibility for its use as an alternative strategy to design, for instance, hierarchical assemblies

of 1D nano-objects into innovative nanocomposites (Kang et al., 2012; Lee et al., 2020; Li and Brant, 2019).

Acknowledgements

The authors acknowledge the European Synchrotron Radiation Facility and the French Collaborating Research Group for the allocation of beamtime on the D2AM beamline under the approved proposal 02-01-880. We thank Nathalie Boudet and Nils Blanc for their assistance during the SAXS experiments, Claire Goldmann for her support in TEM observations and Véronique Peyre for her help with electrophoretic measurements. The present work has benefited from Imagerie-Gif core facility supported by l'Agence Nationale de la Recherche (ANR-11-EQPX-0029/Morphoscope; ANR-10-INBS-04/FranceBioImaging; ANR-11-IDEX-0003-02/ Saclay Plant Sciences). The French Région Ile de France SESAME program is acknowledged for financial support (700 MHz spectrometer).

References

Abend, S., Lagaly, G., 2000. Sol–gel transitions of sodium montmorillonite dispersions. Appl. Clay Sci. 16, 201–227.

Amara, M.-S., Paineau, E., Bacia-Verloop, M., Krapf, M.-E.M., Davidson, P., Belloni, L., Levard, C., Rose, J., Launois, P., Thill, A., 2013. Single-step formation of micron long (OH)3Al2O3Ge(OH) imogolite-like nanotubes. Chem. Commun. 49, 11284–11286. https://doi.org/10.1039/c3cc46839a

Amara, M.S., Paineau, E., Rouziere, S., Guiose, B., Krapf, M.-E.M., Tache, O., Launois, P., Thill, A., 2015. Hybrid, Tunable-Diameter, Metal Oxide Nanotubes for Trapping of Organic Molecules. Chem. Mater. 27, 1488–1494. https://doi.org/10.1021/cm503428q

Arancibia-Miranda, N., Escudey, M., Molina, M., Teresa Garcia-Gonzalez, M., 2011. Use of isoelectric point and pH to evaluate the synthesis of a nanotubular aluminosilicate. J. Non-Cryst. Solids 357, 1750–1756. https://doi.org/10.1016/j.jnoncrysol.2011.01.012

Arancibia-Miranda, N., Escudey, M., Ramirez, R., Gonzalez, R.I., van Duin, A.C.T., Kiwi, M., 2017. Advancements in the Synthesis of Building Block Materials: Experimental Evidence and Modeled Interpretations of the Effect of Na and K on Imogolite Synthesis. J. Phys. Chem. C 121, 12658–12668. https://doi.org/10.1021/acs.jpcc.6b12155

Barrett, S., Budd, P., Price, C., 1991. The Synthesis and Characterization of Imogolite. Eur. Polym. J. 27, 609–612. https://doi.org/10.1016/0014-3057(91)90144-D

Belamie, E., Davidson, P., Giraud-Guille, M.M., 2004. Structure and chirality of the nematic phase in α-chitin suspensions. J. Phys. Chem. B 108, 14991–15000.

Bhattacharjee, S., 2016. DLS and zeta potential–what they are and what they are not? J. Controlled Release 235, 337–351.

Bishop, J.L., Rampe, E.B., Bish, D.L., Abidin, Z., Baker, L.L., Matsue, N., Henmi, T., 2013. Spectral and Hydration Properties of Allophane and Imogolite. Clays Clay Miner. 61, 57–74.
Bousige, C., Rols, S., Paineau, E., Rouziere, S., Mocuta, C., Verberck, B., Wright, J.P., Kataura, H., Launois, P., 2012. Progressive melting in confined one-dimensional C-60 chains. Phys. Rev. B 86, 045446. https://doi.org/10.1103/PhysRevB.86.045446
Cambedouzou, J., Chorro, M., Almairac, R., Noé, L., Flahaut, E., Rols, S., Monthioux, M., Launois, P., 2009. X-ray diffraction as a tool for the determination of the structure of double-walled carbon nanotube batches. Phys. Rev. B 79, 195423.
Camerel, F., Gabriel, J.-C.P., Batail, P., Davidson, P., Lemaire, B., Schmutz, M., Gulik-Krzywicki, T., Bourgaux, C., 2002. Original Single Walled Nanotubules Based on Weakly Interacting Covalent Mineral Polymers, 1∞[Nb2PS10-] in N-Methylformamide. Nano Lett. 2, 403–407.
Carretero, M.I., Pozo, M., 2009. Clay and non-clay minerals in the pharmaceutical industry: Part I. Excipients and medical applications. Appl. Clay Sci. 46, 73–80.
Chemmi, A., Brendle, J., Marichal, C., Lebeau, B., 2015. Key Steps Influencing the Formation of Aluminosilicate Nanotubes by the Fluoride Route. Clays Clay Miner. 63, 132–143. https://doi.org/10.1346/CCMN.2015.0630205
Cradwick, P.D.G., Wada, K., Russell, J., Yoshinaga, N., Masson, C., Farmer, V., 1972. Imogolite, a Hydrated Aluminum Silicate of Tubular Structure. Nat.-Phys. Sci. 240, 187–189.
Davidson, P., Penisson, C., Constantin, D., Gabriel, J.-C.P., 2018. Isotropic, nematic, and lamellar phases in colloidal suspensions of nanosheets. Proc. Natl. Acad. Sci. 115, 6662–6667.
De Braaf, B., Oshima Menegon, M., Paquay, S., Van Der Schoot, P., 2017. Self-organisation of semi-flexible rod-like particles. J. Chem. Phys. 147, 244901.
De Gennes, P.-G., Prost, J., 1993. The physics of liquid crystals. Oxford university press.
Farmer, V., Adams, M., Fraser, A., Palmieri, F., 1983. Synthetic Imogolite - Properties, Synthesis, and Possible Applications. Clay Miner. 18, 459–472. https://doi.org/10.1180/claymin.1983.018.4.11
Farmer, V., Fraser, A., Tait, J., 1977. Synthesis of Imogolite - Tubular Aluminum Silicate Polymer. J. Chem. Soc.-Chem. Commun. 462–463.
Farmer, V.C., Fraser, A.R., 1979. Synthetic imogolite, a tubular hydroxyaluminium silicate, in: Developments in Sedimentology. Elsevier, pp. 547–553.
Farmer, V.C., Fraser, A.R., Tait, J.M., 1979. Characterization of the chemical structures of natural and synthetic aluminosilicate gels and sols by infrared spectroscopy. Geochim. Cosmochim. Acta 43, 1417–1420.
Gabriel, J.-C.P., Sanchez, C., Davidson, P., 1996. Observation of nematic liquid-crystal textures in aqueous gels of smectite clays. J. Phys. Chem. 100, 11139–11143.
Guinier, A., Fournet, G., Yudowitch, K.L., 1955. Small-angle scattering of X-rays.
Gustafsson, J.P., 2001. The surface chemistry of imogolite. Clays Clay Miner. 49, 73–80. https://doi.org/10.1346/CCMN.2001.0490106
Harvey, C.C., Lagaly, G., 2013. Industrial applications, in: Developments in Clay Science. Elsevier, pp. 451–490.
Hemmen, H., Ringdal, N.I., De Azevedo, E.N., Engelsberg, M., Hansen, E.L., Méheust, Y., Fossum, J.O., Knudsen, K.D., 2009. The Isotropic− Nematic Interface in Suspensions of Na− Fluorohectorite Synthetic Clay. Langmuir 25, 12507–12515.
Hentschke, R., Herzfeld, J., 1991. Isotropic, nematic, and columnar ordering in systems of persistent flexible hard rods. Phys. Rev. A 44, 1148.
Holmqvist, P., Alexandridis, P., Lindman, B., 1997. Phase Behavior and Structure of Ternary Amphiphilic Block Copolymer− Alkanol− Water Systems: Comparison of Poly (ethylene oxide)/Poly (propylene oxide) to Poly (ethylene oxide)/Poly (tetrahydrofuran) Copolymers. Langmuir 13, 2471–2479.
Ildefonse, P., Kirkpatrick, R., Montez, B., Calas, G., Flank, A., Lagarde, P., 1994. Al-27 MAS NMR and Aluminum X-Ray Absorption Near-Edge Structure Study of Imogolite and Allophanes. Clays Clay Miner. 42, 276–287. https://doi.org/10.1346/CCMN.1994.0420306

Kajiwara, K., Donkai, N., Fujiyoshi, Y., Inagaki, H., 1986. Lyotropic mesophase of imogolite. 2. Microscopic observation of imogolite mesophase. Makromol. Chem.-Macromol. Chem. Phys. 187, 2895–2907.

Kang, D.-Y., Tong, H.M., Zang, J., Choudhury, R.P., Sholl, D.S., Beckham, H.W., Jones, C.W., Nair, S., 2012. Single-Walled Aluminosilicate Nanotube/Poly(vinyl alcohol) Nanocomposite Membranes. Acs Appl. Mater. Interfaces 4, 965–976. https://doi.org/10.1021/am201614w

Kato, T., Uchida, J., Ichikawa, T., Sakamoto, T., 2018. Functional liquid crystals towards the next generation of materials. Angew. Chem. Int. Ed. 57, 4355–4371.

Kieffer, J., Karkoulis, D., 2013. PyFAI, a versatile library for azimuthal regrouping, in: Journal of Physics: Conference Series. IOP Publishing, p. 202012.

Kleshchanok, D., Meijer, J.-M., Petukhov, A.V., Portale, G., Lekkerkerker, H.N., 2012. Sedimentation and depletion attraction directing glass and liquid crystal formation in aqueous platelet/sphere mixtures. Soft Matter 8, 191–197.

Kleshchanok, D., Petukhov, A.V., Holmqvist, P., Byelov, D.V., Lekkerkerker, H.N., 2010. Structures and phase behavior in mixtures of charged colloidal spheres and platelets. Langmuir 26, 13614–13621.

Lee, H., Jeon, Y., Lee, Y., Lee, S.U., Takahara, A., Sohn, D., 2014. Thermodynamic Control of Diameter-Modulated Aluminosilicate Nanotubes. J. Phys. Chem. C 118, 8148–8152. https://doi.org/10.1021/jp411725z

Lee, W.J., Paineau, E., Anthony, D.B., Gao, Y., Leese, H.S., Rouzière, S., Launois, P., Shaffer, M.S.P., 2020. Inorganic Nanotube Mesophases Enable Strong Self-Healing Fibers. ACS Nano 14, 5570–5580.

Levard, C., Masion, A., Rose, J., Doelsch, E., Borschneck, D., Olivi, L., Chaurand, P., Dominici, C., Ziarelli, F., Thill, A., Maillet, P., Bottero, J.Y., 2011. Synthesis of Ge-imogolite: influence of the hydrolysis ratio on the structure of the nanotubes. Phys. Chem. Chem. Phys. 13, 14516–14522.

Levard, C., Rose, J., Masion, A., Doelsch, E., Borschneck, D., Olivi, L., Dominici, C., Grauby, O., Woicik, J.C., Bottero, J.-Y., 2008. Synthesis of large quantities of single-walled aluminogermanate nanotube. J. Am. Chem. Soc. 130, 5862–5863. https://doi.org/10.1021/jaB01045a

Levard, C., Rose, J., Thill, A., Masion, A., Doelsch, E., Maillet, P., Spalla, O., Olivi, L., Cognigni, A., Ziarelli, F., Bottero, J.-Y., 2010. Formation and Growth Mechanisms of Imogolite-Like Aluminogermanate Nanotubes. Chem. Mater. 22, 2466–2473.

Levitz, P., Zinsmeister, M., Davidson, P., Constantin, D., Poncelet, O., 2008. Intermittent Brownian dynamics over a rigid strand: Heavily tailed relocation statistics in a simple geometry. Phys. Rev. E 78, 030102. https://doi.org/10.1103/PhysRevE.78.030102

Li, M., Brant, J.A., 2019. Effects of aluminogermanate imogolite nanotube orientation on mass transport across polyamide nanocomposite membranes. J. Membr. Sci. 585, 38–51.

Liao, Y., Picot, P., Brubach, J.-B., Roy, P., Le Caër, S., Thill, A., 2018. Self-supporting thin films of imogolite and imogolite-like nanotubes for infrared spectroscopy. Appl. Clay Sci. 164, 58–67.

Liao, Y.-Y., Picot, P., Brubach, J.-B., Roy, P., Thill, A., Le Caer, S., 2019. Water Adsorption in Single-and Double-Walled Inorganic Nanotubes. J. Phys. Chem. C 123, 19768–19777.

Luo, Z., Song, H., Feng, X., Run, M., Cui, H., Wu, L., Gao, J., Wang, Z., 2013. Liquid crystalline phase behavior and sol–gel transition in aqueous halloysite nanotube dispersions. Langmuir 29, 12358–12366.

Maier, E.E., Krause, R., Deggelmann, M., Hagenbuechle, M., Weber, R., Fraden, S., 1992. Liquidlike order of charged rodlike particle solutions. Macromolecules 25, 1125–1133.

Maillet, P., Levard, C., Larquet, E., Mariet, C., Spalla, O., Menguy, N., Masion, A., Doelsch, E., Rose, J., Thill, A., 2010. Evidence of Double-Walled Al-Ge Imogolite-Like Nanotubes. A Cryo-TEM and SAXS Investigation. J. Am. Chem. Soc. 132, 1208–1209.

Massiot, D., Fayon, F., Capron, M., King, I., Le Calvé, S., Alonso, B., Durand, J.-O., Bujoli, B., Gan, Z., Hoatson, G., 2002. Modelling one-and two-dimensional solid-state NMR spectra. Magn. Reson. Chem. 40, 70–76.

644 Michot, L.J., Bihannic, I., Maddi, S., Baravian, C., Levitz, P., Davidson, P., 2008. Sol/gel and
645 isotropic/nematic transitions in aqueous suspensions of natural nontronite clay. Influence of
646 particle anisotropy. 1. Features of the I/N transition. Langmuir 24, 3127–3139.
647 Michot, L.J., Bihannic, I., Maddi, S., Funari, S.S., Baravian, C., Levitz, P., Davidson, P., 2006. Liquid–
648 crystalline aqueous clay suspensions. Proc. Natl. Acad. Sci. 103, 16101–16104.
649 Michot, L.J., Bihannic, I., Porsch, K., Maddi, S., Baravian, C., Mougel, J., Levitz, P., 2004. Phase diagrams
650 of Wyoming Na-montmorillonite clay. Influence of particle anisotropy. Langmuir 20, 10829–
651 10837.
652 Michot, L.J., Paineau, E., Bihannic, I., Maddi, S., Duval, J.F.L., Baravian, C., Davidson, P., Levitz, P., 2013.
653 Isotropic/nematic and sol/gel transitions in aqueous suspensions of size selected nontronite
654 NAul. Clay Miner. 48, 663–685. https://doi.org/10.1180/claymin.2013.048.5.01
655 Miyamoto, N., Iijima, H., Ohkubo, H., Yamauchi, Y., 2010. Liquid crystal phases in the aqueous colloids
656 of size-controlled fluorinated layered clay mineral nanosheets. Chem. Commun. 46, 4166–
657 4168.
658 Miyamoto, N., Nakato, T., 2012. Liquid crystalline inorganic nanosheet colloids derived from layered
659 materials. Isr. J. Chem. 52, 881–894.
660 Monet, G., Amara, M.S., Rouzière, S., Paineau, E., Chai, Z., Elliott, J.D., Poli, E., Liu, L.-M., Teobaldi, G.,
661 Launois, P., 2018. Structural resolution of inorganic nanotubes with complex stoichiometry.
662 Nat. Commun. 9.
663 Mourchid, A., Delville, A., Lambard, J., Lecolier, E., Levitz, P., 1995. Phase diagram of colloidal
664 dispersions of anisotropic charged particles: equilibrium properties, structure, and rheology of
665 laponite suspensions. Langmuir 11, 1942–1950.
666 Olphen, H. van, 1977. An introduction to clay colloid chemistry, for clay technologists, geologists, and
667 soil scientists.
668 Onsager, L., 1949. The effects of shape on the interaction of colloidal particles. Ann. N. Y. Acad. Sci. 51,
669 627–659.
670 Paineau, E., 2018. Imogolite Nanotubes: A Flexible Nanoplatform with Multipurpose Applications.
671 Appl. Sci. 8, 1921.
672 Paineau, E., Amara, M.S., Monet, G., Peyre, V., Rouzière, S., Launois, P., 2017. Effect of Ionic Strength
673 on the Bundling of Metal Oxide Imogolite Nanotubes. J. Phys. Chem. C 121, 21740–21749.
674 Paineau, E., Antonova, K., Baravian, C., Bihannic, I., Davidson, P., Dozov, I., Imperor-Clerc, M., Levitz,
675 P., Madsen, A., Meneau, F., Michot, L.J., 2009. Liquid-Crystalline Nematic Phase in Aqueous
676 Suspensions of a Disk-Shaped Natural Beidellite Clay. J. Phys. Chem. B 113, 15858–15869.
677 Paineau, E., Krapf, M.-E.M., Amara, M.-S., Matskova, N.V., Dozov, I., Rouziere, S., Thill, A., Launois, P.,
678 Davidson, P., 2016. A liquid-crystalline hexagonal columnar phase in highly-dilute suspensions
679 of imogolite nanotubes. Nat. Commun. 7, 10271.
680 Paineau, E., Launois, P., 2019. Nanomaterials From Imogolite: Structure, Properties, and Functional
681 Materials, in: Nanomaterials from Clay Minerals. Elsevier, pp. 257–284.
682 Paineau, E., Monet, G., Peyre, V., Goldmann, C., Rouzière, S., Launois, P., 2019. Colloidal Stability of
683 Imogolite Nanotube Dispersions: A Phase Diagram Study. Langmuir 35, 12451–12459.
684 Paineau, E., Philippe, A.M., Antonova, K., Bihannic, I., Davidson, P., Dozov, I., Gabriel, J.C.P., Imperor-
685 Clerc, M., Levitz, P., Meneau, F., Michot, L.J., 2013. Liquid-crystalline properties of aqueous
686 suspensions of natural clay nanosheets. Liq. Cryst. Rev. 1, 110–126.
687 Picot, P., Liao, Y., Barruet, E., Gobeaux, F., Coradin, T., Thill, A., 2018. Exploring Hybrid Imogolite
688 Nanotube Formation via Si/Al Stoichiometry Control. Langmuir 34, 13225–13234.
689 Poli, E., Elliott, J., Chulkov, S.K., Watkins, M.B., Teobaldi, G., 2019. The role of cation-vacancies for the
690 electronic and optical properties of aluminosilicate imogolite nanotubes: a non-local, linear-
691 response TDDFT study. Front. Chem. 7, 210.
692 Poncelet, O.J., 2002. Method to prepare an aluminosilicate polymer. Google Patents.
693 Rosenfeldt, S., Stöter, M., Schlenk, M., Martin, T., Albuquerque, R.Q., Förster, S., Breu, J., 2016. In-
694 Depth Insights into the Key Steps of Delamination of Charged 2D Nanomaterials. Langmuir 32,
695 10582–10588.

Ruzicka, B., Zaccarelli, E., Zulian, L., Angelini, R., Sztucki, M., Moussaïd, A., Narayanan, T., Sciortino, F., 2011. Observation of empty liquids and equilibrium gels in a colloidal clay. Nat. Mater. 10, 56.

Schindelin, J., Arganda-Carreras, I., Frise, E., Kaynig, V., Longair, M., Pietzsch, T., Preibisch, S., Rueden, C., Saalfeld, S., Schmid, B., 2012. Fiji: an open-source platform for biological-image analysis. Nat. Methods 9, 676.

Su, C.-Y., Lyu, Q., Kang, D.-Y., Yang, Z.-H., Lam, C.H., Chen, Y.-H., Lo, S.-C., Hua, C.-C., Lin, L.-C., 2019. Hexagonal Superalignment of Nano-Objects with Tunable Separation in a Dilute and Spacer-Free Solution. Phys. Rev. Lett. 123, 238002.

Tani, M., Liu, C., Huang, P.M., 2004. Atomic force microscopy of synthetic imogolite. Geoderma 118, 209–220. https://doi.org/10.1016/S0016-7061(03)00204-0

Teobaldi, G., Beglitis, N.S., Fisher, A.J., Zerbetto, F., Hofer, A.A., 2009. Hydroxyl vacancies in single-walled aluminosilicate and aluminogermanate nanotubes. J. Phys.-Condens. Matter 21, 195301. https://doi.org/10.1088/0953-8984/21/19/195301

Thill, A., Maillet, P., Guiose, B., Spalla, O., Belloni, L., Chaurand, P., Auffan, M., Olivi, L., Rose, J., 2012. Physico-chemical Control over the Single- or Double-Wall Structure of Aluminogermanate Imogolite-like Nanotubes. J. Am. Chem. Soc. 134, 3780–3786.

Thomas, B., Coradin, T., Laurent, G., Valentin, R., Mouloungui, Z., Babonneau, F., Baccile, N., 2012. Biosurfactant-mediated one-step synthesis of hydrophobic functional imogolite nanotubes. Rsc Adv. 2, 426–435. https://doi.org/10.1039/c1ra00442e

Wada, S., Wada, K., 1982. Effects of substitution of germanium for silicon in imogolite. Clays Clay Miner. 30, 123–128.

Watanabe, J., Sakajiri, K., Okoshi, K., Kawauchi, S., Magoshi, J., 2001. Columnar Liquid Crystals in Polypeptides, 1. Columnar Hexagonal Phase Observed in Lyotropic Solutions of Poly (γ-octadecyl-L-glutamate) Dissolved in Amphiphilic Solvents, Such as Octadecylamine, Octadecyl Alcohol, and Octadecanoic Acid. Macromol. Chem. Phys. 202, 1004–1009.

Wensink, H.H., 2007. Columnar versus smectic order in systems of charged colloidal rods. J. Chem. Phys. 126, 194901.

Wilson, M.A., Lee, G.S.H., Taylor, R.C., 2001. Tetrahedral rehydration during imogolite formation. J. Non-Cryst. Solids 296, 172–181. https://doi.org/10.1016/S0022-3093(01)00908-5

Woolston, P., van Duijneveldt, J.S., 2015. Isotropic-nematic phase transition in aqueous sepiolite suspensions. J. Colloid Interface Sci. 437, 65–70. https://doi.org/10.1016/j.jcis.2014.09.014

Yoshinaga, N., Aomine, S., 1962. Imogolite in some Ando soils. Soil Sci. Plant Nutr. 8, 22–29.

Yucelen, G.I., Choudhury, R.P., Leisen, J., Nair, S., Beckham, H.W., 2012a. Defect Structures in Aluminosilicate Single-Walled Nanotubes: A Solid-State Nuclear Magnetic Resonance Investigation. J. Phys. Chem. C 116, 17149–17157. https://doi.org/10.1021/jp3059728

Yucelen, G.I., Kang, D.-Y., Guerrero-Ferreira, R.C., Wright, E.R., Beckham, H.W., Nair, S., 2012b. Shaping Single-Walled Metal Oxide Nanotubes from Precursors of Controlled Curvature. Nano Lett. 12, 827–832. https://doi.org/10.1021/nl203880z

Zanzottera, C., Vicente, A., Armandi, M., Fernandez, C., Garrone, E., Bonelli, B., 2012. Thermal Collapse of Single-Walled Alumino-Silicate Nanotubes: Transformation Mechanisms and Morphology of the Resulting Lamellar Phases. J. Phys. Chem. C 116, 23577–23584. https://doi.org/10.1021/jp3090638

Zhang, Z.X., van Duijneveldt, J.S., 2006. Isotropic-nematic phase transition of nonaqueous suspensions of natural clay rods. J. Chem. Phys. 124, 154910.